

Direct inelastic scattering of N₂ from Ag(111). I. Rotational populations and alignment

Greg O. Sitz, Andrew C. Kummel, and Richard N. Zare

Department of Chemistry, Stanford University, Stanford, California 94305

(Received 22 February 1988; accepted 11 May 1988)

The rotational state populations and the quadrupole and hexadecapole alignment moments of N₂ scattered off clean Ag(111) are determined by resonance enhanced multiphoton ionization (REMPI). The scattered N₂ is found to be highly aligned with its rotational angular momentum vector \mathbf{J} parallel to the surface. The degree of alignment is found to increase with increasing rotational excitation. We see less than perfect alignment at intermediate J values indicating that the surface is not completely flat. The alignment is relatively insensitive to incident energy, incident angle, or surface temperature T_s . However, the rotational state population distributions show pronounced rainbows for higher incident energy and/or more grazing exit angle. The rotational state distributions are found to depend strongly on the final scattering angle at low T_s ; this effect is markedly reduced at higher T_s . Time-of-flight measurements are used to determine the average velocity of the scattered N₂ as a function of rotational level. It is found that higher rotational excitation correlates with lower average velocity and that the incident molecules lose 20%–30% of their translational energy to the solid. No correlation is found between velocity and alignment. A comparison is made with published results for the NO/Ag(111) system and a variety of theoretical models found in the literature.

I. INTRODUCTION

Rotationally inelastic scattering has proven to be a valuable technique for understanding the microscopic dynamics of gas–surface interactions. This is particularly true when the quantum state distributions of the scattered molecules are not equilibrated with the surface. For directly scattered molecules, rotational state distributions relate to the degree of anisotropy of the gas–surface potential with respect to the orientation of the molecular figure axis.¹ Moreover, measurements of the polarization of the angular momentum of the scattered molecules provide information on the directionality of this anisotropy.²

Many groups have reported rotational state distributions of molecules scattered or desorbed from solid surfaces; for recent reviews see Barker and Auerbach,³ Cavanagh and King,⁴ and Ertl and Lin.⁵ There are two main techniques used for studying rotationally inelastic scattering. The first involves use of a mass spectrometer as a detector and relies on resolving the different rotational transitions in angle and/or time. To date, this technique has been applied only to hydrogen and its isotopic variants. The second technique utilizes optical (commonly laser based) spectroscopy to probe directly the quantum state distributions of the scattered molecules. This approach is generally applicable, although it may prove difficult in some cases because of lack of a suitable spectroscopic scheme.

Most laser based studies involve the interactions of nitric oxide with a variety of surfaces. This is because NO can be easily detected in a quantum state selective manner compared with other stable diatomic or polyatomic molecules. Since the initial effusive beam experiments,⁶ two groups have compiled an extensive amount of data on the NO/Ag(111) system using supersonic molecular beam sources.

Kleyn, Luntz, and Auerbach (KLA)^{7–10} have concentrated on scattering at higher incident beam energies (0.3–1.2 eV), whereas Kubiak *et al.*¹¹ performed experiments at lower energies (0.05–0.3 eV). Both groups observed rainbows in the scattered rotational distribution; this feature becomes more pronounced at higher incident energies. Both groups observed substantial excitation of the low-lying ²Π_{3/2} fine structure state of NO, which is absent in the incident beam because of cooling in the supersonic expansion. Kubiak *et al.*^{6,11} observed differences in the rotational state populations for the two fine structure states and suggest the possibility of scattering on two different potential curves. Luntz *et al.*¹² observed unequal Λ-doublet populations at high NO rotational excitation. Once more this indicates that the scattering involves more than one potential energy surface.

In addition to determining the rotational population distribution, KLA^{9,10} reported a measurement of the polarization of the scattered NO, that is, information on the spatial distribution of the NO rotational angular momentum vectors. They measured b_2/b_0 , where b_i is the i th coefficient for an expansion of the angular momentum distribution in Legendre polynomials. They found $b_2/b_0 \sim 0$ for low J (< 10.5) increased smoothly to ~ -1.75 for intermediate J ($20.5 < J < 35.5$) and decreased to zero for the highest J values measured ($\gtrsim 40.5$). The negative value for b_2/b_0 indicates a tendency for the molecule to rotate with its angular momentum vector \mathbf{J} lying in a plane parallel to the surface. The range of b_2/b_0 values spans +5.0 to –2.5, with –2.5 corresponding to perfect alignment of \mathbf{J} parallel to the surface.

There is only one other report of a direct measurement of alignment in surface scattering. Jacobs *et al.*¹³ recently observed a small positive alignment ($\langle \mathbf{J} \parallel \hat{\mathbf{n}} \rangle$) for higher rota-

tional levels of NO desorbing from Pt(111). In addition, there have been indirect measurements of polarization effects in gas-surface scattering studied by magnetic field induced changes on bulk transport reported by Hermans *et al.*¹⁴ Their results are qualitative owing to the uncharacterized surfaces used and the indirect measure of the polarization, but they do indicate the influence of tangential forces, i.e., forces in the plane of the surface.

One aspect which both complicates and enriches the study of NO scattering is the fact that NO is an open-shell molecule, that is, a free radical. The unpaired electron leads to a relatively strong attractive interaction with most metal surfaces. This makes direct scattering experiments at low surface temperatures more difficult and introduces the theoretical complication of scattering on multiple potential curves. We were partially motivated to undertake a study of a different molecule, in this case N₂, in order to discount the role of this structure in the scattering process. N₂ is advantageous because it has a closed-shell electronic ground state and interacts weakly with the Ag(111) substrate, allowing for direct scattering experiments over a wide range of surface temperatures.

Scattering of N₂ from Ag(100) has been studied experimentally by Muhlhausen *et al.*,¹⁵ and from Ag(111) by Asada,¹⁶ and by Asada and Matsui,¹⁷ where it was found that the scattering was direct with angular distributions peaked near specular. Muhlhausen *et al.*^{15,18} were able to model their angular and velocity distributions quite well over a wide range of incident energies, incident angles, and surface temperatures using a Generalized Langevin Equation (GLE) which attempts to include all the classical degrees of freedom. However, they concluded that their measurements were insensitive to rotational inelasticity and pointed out the need for direct experiments in this area.

In this paper, we report the results of a study of the rotationally inelastic scattering of N₂ from Ag(111). This paper represents a more complete account of work already briefly reported.^{19,20} The rotational state distributions and the degree of alignment of the rotational angular momentum for a variety of initial conditions have been measured. We observe strong alignment of **J** parallel to the surface plane. The degree of alignment tends to increase with the rotational quantum number. There are pronounced rainbows in the rotational state populations for incident translational energies in the range of 0.2–0.4 eV. The rainbow structure becomes more pronounced with increasing incident energy. We compare our results with published data for NO/Ag(111) and with calculations found in the literature.

II. EXPERIMENTAL APPARATUS

The apparatus used in these experiments is shown schematically in Fig. 1. Various aspects of this setup have been described in previous publications^{11,20,21}; however, some significant changes have been incorporated and will be detailed here.

A. Main chamber

The main chamber is a two-tiered stainless steel vessel pumped by a 10 in. liquid nitrogen trapped oil diffusion

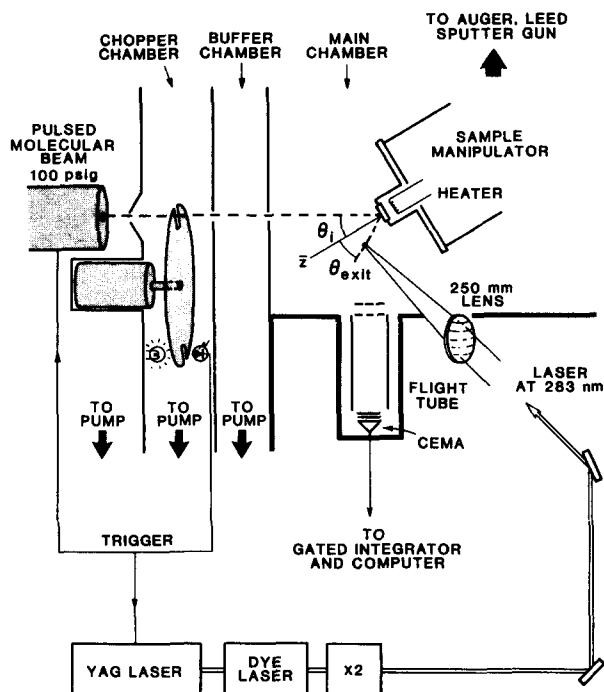


FIG. 1. Schematic diagram of the molecular beam surface scattering apparatus used in the study of the scattering of N₂ from Ag(111).

pump (CVC 10). The upper tier houses the LEED, Auger, and sputtering facilities, and the scattering experiments are performed in the lower tier. The crystal is translated between levels by means of a long stroke bellows manipulator. Mounted in the lower tier is a quadrupole mass spectrometer (VG SX200) which lies on the molecular beam axis and is used for beam diagnostics as well as residual gas analysis. The base pressure of the main chamber is typically $3\text{--}4 \times 10^{-10}$ Torr and increases by less than 2×10^{-11} Torr during a scattering experiment.

B. Crystal manipulator

The crystal manipulator head consists of a cylindrical copper block with a spiral cut in it for efficient coolant flow. The crystal is attached to the top of a hat which is clamped by the brim to one end of the cooling block. The hat is separated from the cooling block by a sapphire washer for electrical insulation and thermal insulation at high temperature. The surface is heated via electron bombardment by a filament located just behind the sample holder.

The Ag(111) sample (Aremco Inc.) was prepared by standard techniques and brazed onto the copper support. Prior to brazing, two 0.02 in. diameter holes were electron discharge milled 3/8 in. deep into the copper support, parallel to the front face. Two chromel–alumel thermocouples were inserted in these holes for sample temperature measurement.

Experiments have been performed for surface temperatures between 90 and 700 K. At lower temperatures the crystal is flashed to 700 K every 30–45 min to remove any contaminants that may have adsorbed to the surface. To test our sensitivity to contaminant buildup, experiments were conducted over several hours at low T , without flashing. The

primary effect was simply to reduce the scattered intensity ($\sim 10\%/h$) but not to change the population or alignment distributions. Presumably, those molecules that interact with impurities are scattered diffusely in space and time. Consequently, they are discriminated against in detection.

The entire manipulator head can be rotated about three orthogonal axes, two of which intersect the center of the front face of the crystal. The manipulator design employs a goniometer mechanism to achieve the in-plane tilt so that all mechanical parts are always behind the crystal surface. An advantage of this is that there is no line of sight from the manipulator to the sample surface which reduces the possibility of contaminating the surface from outgassing during flashes to high temperature. The crystal can also be translated in three dimensions. Initial alignment is performed by replacing the molecular beam source with a He-Ne laser and adjusting the manipulator angles until the reflected laser beam passes back through the final molecular beam collimator. This procedure is accomplished with the system under vacuum. Azimuthal alignment was checked using LEED. All experiments reported here were performed with the molecular beam incident along the [211] azimuth of the (111) surface.

C. Beam source

The molecular beam source employs a commercial pulsed valve (General Valve series 9) mounted on a flange which allows for three orthogonal linear translations for precise beam alignment. The source chamber is pumped by an unbaffled 6 in. diffusion pump equipped with a Mexican cold hat (Varian VHS-6). The nozzle orifice is 400 μm in diame-

ter. Some experiments were done with a 150 μm diameter nozzle; this change had no effect on any of the measured distributions.

The beam is collimated by a 2 mm diameter skimmer located ~ 1 cm from the nozzle orifice and enters the first buffer chamber, which is pumped by a water baffled 4 in. diffusion pump (CVC PMP-4B). This chamber contains a mechanical chopper running at 200 Hz which reduces the background gas load on the main chamber and provides a sharp temporal profile for time-of-flight (TOF) measurements. For TOF measurements the chopper speed is increased to 300 Hz. By selecting a small window (~ 12 – 15 μs) in the center of the valve pulse (~ 1 ms in duration), any problems related to different incident beam distributions at the beginning or end of the pulse can be avoided.¹⁹ The chopper mount is equipped with an LED-photodiode combination to provide a synchronization pulse for the laser. The chopper motor is mounted in a tube invaginated into the source chamber in order to minimize the source of crystal distance by keeping the buffer chamber thin.

Following the chopper motor chamber is a second differentially pumped buffer chamber, evacuated by a water baffled 4 in. diffusion pump (Varian VHS-4). The collimating aperture at the exit of this chamber is 3 mm in diameter and defines the beam size, which is ~ 4 mm in diameter on the sample surface at normal incidence. The total distance from the nozzle to the crystal is 15.9 cm.

D. Laser source

N_2 is detected in a quantum state specific manner by $2 + 2$ resonance enhanced multiphoton ionization

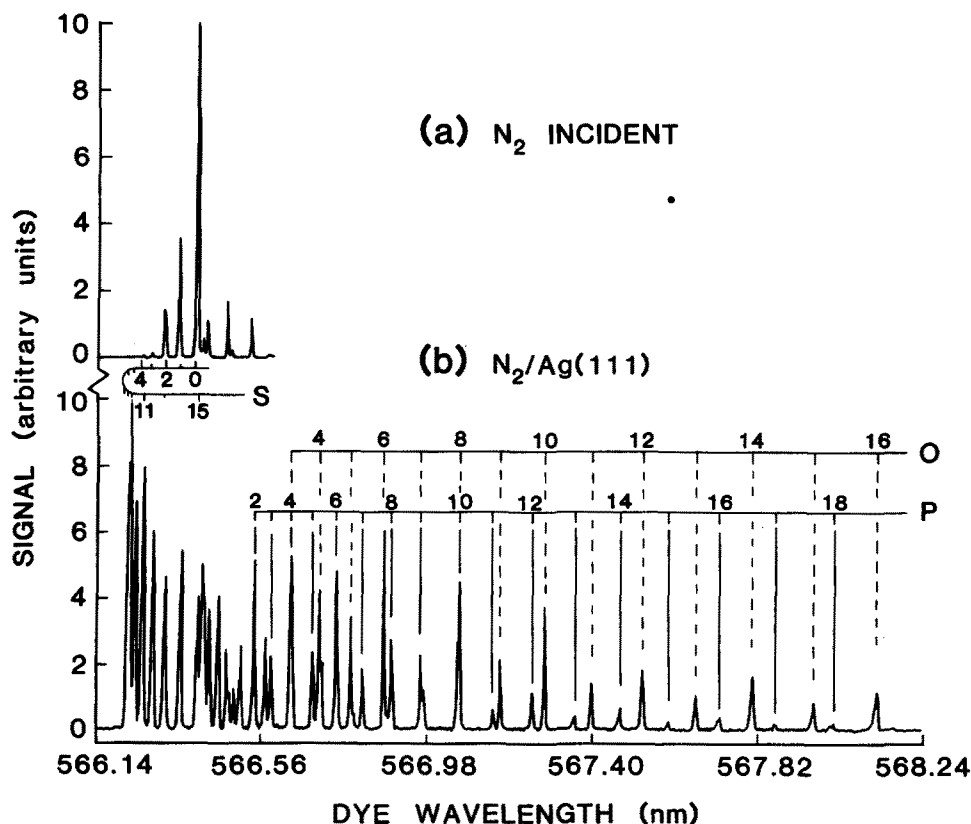


FIG. 2. REPMI spectra of (a) the incident beam and (b) the scattered beam. Conditions were: in (a) nozzle orifice $d = 400$ μm , stagnation pressure $p_0 = 70$ psig, seeding ratio of 22% N_2 and 78% H_2 , and in (b) $\theta_i = 15^\circ$, $\theta_f = 20^\circ$, and $T_s = 90$ K. Line assignments are made based on tabulated energy levels (Ref. 24).

(REMPI).^{20,23} Tunable radiation used to excite the (1,0) band of the two-photon $a^1\Pi_g-X^1\Sigma_g^+$ transition in N₂ at 283–285 nm is generated by frequency doubling the output of a Nd³⁺:YAG pumped dye laser (Quantel YGC581C-TDL50-UVX2). The UV light is separated from the residual green fundamental by multiple reflections off dichroic mirrors (CVI). The same color used to excite the initial two-photon transition also ionizes the excited molecules. The dye laser is operated with a mix of rhodamine 590 and 610 (~7:1) optimized to provide a flat output power between 566 and 570 nm. The variation in power is measured to be less than 5% across this region; therefore, the measured signals are not corrected for the change of the laser energy with laser wavelength. Typical pulse energies are 13–16 mJ per pulse at 283 nm, measured at the entrance to the chamber.

The laser beam is focused between the grids of a time-of-flight mass spectrometer by a 20 cm focal length AR coated lens. The lens is mounted 1 cm off the center line of a rotating mount, the axis of which is parallel to the front face of the Ag(111) crystal. This arrangement allows different final scattering angles to be probed by rotating the lens and making minor adjustment to the final steering prism. The focal point is accurately positioned along the laser propagation direction by translating the whole lens assembly by means of a micrometer driven linear stage. The laser propagates perpendicular to the plane defined by the molecular beam and the surface normal and is focused 1 cm from the surface. The combination of molecular beam spot size on the sample (4 mm) and distance to the probe volume (1 cm) gives an angular acceptance of ~15° at normal incidence. However, our angular resolution, in the sense of being able to observe differences in the distributions, is better than this; namely, it is closer to 10°.

The laser beam is linearly polarized, and the direction of polarization is varied with respect to the surface normal by means of a double Fresnel rhomb (Carl Lambrecht) or a half-wave plate (Special Optics) held in a precision rotating mount positioned just before the focusing lens. The degree of polarization is frequently checked by means of a Glan-Thompson prism and is always greater than 99.5% and typically greater than 99.8%. The possibility of strain-induced birefringence in the window was checked by analyzing the polarization of the light after exiting the chamber through a second window. By evacuating the chamber, and thus stressing the window as a result of the pressure difference, the percentage of linear polarization is reduced from 99.9% to 99.8%. This change is negligible in our experiment.

Ions formed at the laser focus are collected in a time-of-flight mass spectrometer and detected with a multichannel plate (Galileo CEMA).²¹ Ion signal collection, laser wavelength, and laser polarization are all computer controlled via CAMAC interfaced to a DEC PDP 11/23 computer.

III. RESULTS AND DISCUSSION

A. Rotational excitation

Figure 2(a) shows a REMPI spectrum of the incident beam; the scattered beam is shown in Fig. 2(b). The spectra are for an incident energy $E_i = 0.3$ eV, an incident angle θ_i

TABLE I. Incident beam rotational state populations for beam energies and expansion conditions used in this study.

	Incident energy			
	0.1 eV	0.2 eV	0.3 eV	0.4 eV
J				
0	0.460	0.493	0.458	0.452
1	0.306	0.333	0.355	0.299
2	0.208	0.144	0.162	0.148
3	0.013	0.016	0.016	0.042
4	0.012	0.014	0.009	0.058
$\langle E_r \rangle$ (cm ⁻¹)	4.6	4.0	4.1	6.3
$p_0 d$ (Torr cm)	67	67	180	67

= 15° (measured with respect to the surface normal), an exit angle $\theta_f = 20^\circ$, and a surface temperature $T_s = 90$ K. The spectral assignments are made based on energy levels determined by Vanderslice, Tilford, and Wilkerson.²⁴ Assignment of a rotational temperature to the incident beam of Fig. 2(a) is somewhat ambiguous since the rotational distribution is not Boltzmann; therefore, we list in Table I the actual level populations and average rotational energies for the four beam energies used in this study.

Since ¹⁴N has nuclear spin of 1, N₂ has ortho and para-nuclear spin states which match up with even and odd rotational levels (with statistical weights of 6 and 3, respectively). Generally, these are not collisionally mixed either in the supersonic molecular beam expansion or (presumably) by subsequent collision with the surface. Thus, the experiment can be conceptually divided into two parts, one with ortho N₂ in even rotational levels, the other with para N₂ in odd rotational levels. In none of our results do we see any systematic differences in the scattering for the two groups of molecules.

B. Alignment

1. Measurements and fits

The spectrum of the scattered beam in Fig. 2(b) shows considerable rotational excitation and substantially different intensities for transitions in different branches originating from the same ground state level compared to a similar spectrum of isotropic background gas.²⁰ The cause of the intensity variation is polarization of the sample, and this must be quantified in order to interpret the line intensities in a spectrum.²⁵

Polarization is generally described in terms of the multipole moments of the angular momentum distribution,²⁶ defined by

$$P(J, M) = n(J) \sum_{k, q} \xi(k) A_{q\pm}^{(k)}(J) [(JM | J_{q\pm}^{(k)} | JM) / J^k], \quad (1)$$

where $P(J, M)$ is the probability of being in the state (J, M) , $n(J)$ is the population, $\xi(k)$ is a normalization constant,²⁵ and at high J the $(JM | J_{q\pm}^{(k)} | JM)$ are proportional to the real spherical harmonics $Y_{q\pm}^{(k)}(\theta, \phi)$, i.e., the more familiar terms used by chemists in speaking of s, p , and d orbitals. The $A_{q\pm}^{(k)}$ are the moments and describe the extent to which the

distribution looks like the corresponding $Y_{q\pm}^{(k)}$ term.²⁷ A sample is said to be aligned if states with high $|M|$ are more populated than those with low $|M|$ or vice versa. An aligned sample would have nonzero $A_{q\pm}^{(k)}$ with k even. A sample is oriented if there is a difference in population between states with $+M$ compared to those with $-M$ and would have nonzero $A_{q\pm}^{(k)}$ with k odd. A completely unpolarized sample would have only one nonzero polarization moment, $A_{0+}^{(0)}$ which relates to the population (see below). This paper is concerned only with alignment. Because linearly polarized light is used, the measurement is insensitive to any orientation that may be present. The orientation moments are the subject of other papers.^{29,30}

The intensity for two-photon excitation with linearly polarized light can be written as²⁵

$$I(\theta; J_i, J_f) = n(J_i) C(\det) \{ A_{0+}^{(0)}(J_i, \text{apparent}) P_{0+}^{(0)}(J_i, J_f) + A_{0+}^{(2)}(J_i, \text{apparent}) P_{0+}^{(2)}(\theta; J_i, J_f) + A_{1+}^{(2)}(J_i, \text{apparent}) P_{1+}^{(2)}(\theta; J_i, J_f) + A_{0+}^{(4)}(J_i, \text{apparent}) P_{0+}^{(4)}(\theta; J_i, J_f) + A_{1+}^{(4)}(J_i, \text{apparent}) P_{1+}^{(4)}(\theta; J_i, J_f) \}, \quad (2)$$

where the $P_{q+}^{(k)}(\theta; J_i, J_f)$ are the moments of the line strength and the $A_{q+}^{(k)}(J_i, \text{apparent})$ are the moments of the angular momentum distribution describing the rotational level J_i . Note that Eq. (2) is general and does not assume cylindrical symmetry. The moments appearing in Eq. (2) are "apparent" moments; they arise as a result of the fact that for a fixed probe laser propagation direction the contribution of all the real moments of the distribution are not distinguishable because the various sets of the line strengths are not linearly independent. For example, the $A_{0+}^{(2)}(J_i, \text{apparent})$ moment may include contributions from the real $A_{0+}^{(2)}(J_i)$, $A_{2+}^{(2)}(J_i)$, $A_{2+}^{(4)}(J_i)$, and $A_{4+}^{(4)}(J_i)$ moments. This will be discussed in greater detail in the Appendix where we will show that the contribution to Eq. (2) to the noncylindrically symmetric moments is small.

In the limit that the angular momentum distribution of the scattered beam is cylindrically symmetric about the surface normal, Eq. (2) reduces to

$$I(\theta; J_i, J_f) = n(J_i) C(\det) \{ A_{0+}^{(0)}(J_i) P_{0+}^{(0)}(J_i, J_f) + A_{0+}^{(2)}(J_i) P_{0+}^{(2)}(\theta; J_i, J_f) + A_{0+}^{(4)}(J_i) P_{0+}^{(4)}(\theta; J_i, J_f) \}, \quad (3)$$

where the moments are now the real moments of the distribution. Specifically, the first term in Eq. (3), $n(J_i) C(\det) A_{0+}^{(0)}(J_i)$, is simply related to the population since the monopole moment $A_{0+}^{(0)}(J_i)$ is identically equal to 1. For future reference we will define

$$a_{0+}^{(0)} = n(J_i) C(\det) A_{0+}^{(0)} \equiv n(J_i) C(\det)$$

and call this term the population. $a_{0+}^{(0)}$ has no angular dependence; hence, this term represents the isotropic part of the distribution. $A_{0+}^{(2)}$ is the quadrupole and $A_{0+}^{(4)}$ the hexadecapole moment; they provide information on the spatial distribution of the angular momentum vector \mathbf{J}_i , i.e., on the M

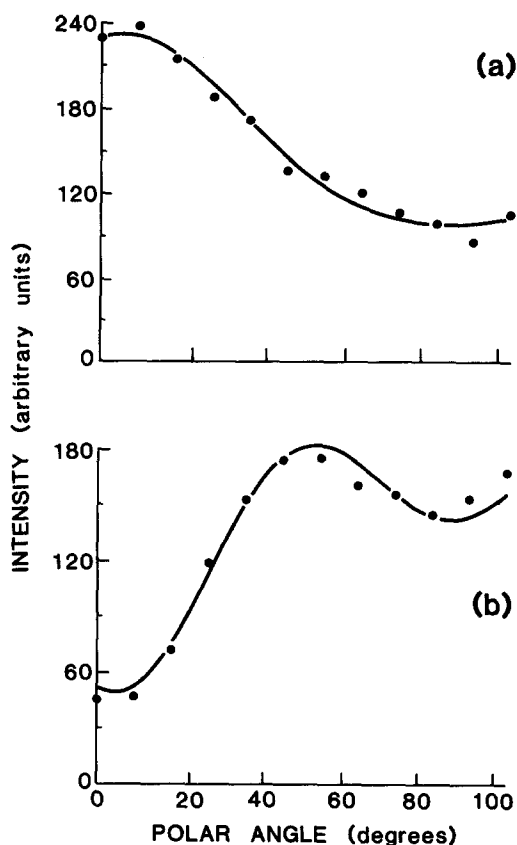


FIG. 3. REMPI integrated line intensities vs laser polarization angle for (a) $O(15)$ and (b) for $P(15)$ for the conditions of Fig. 2. The laser polarization angle is measured with respect to the surface normal. The symbols are the measured data points, and the solid curves are least-squares fits to Eq. (3) yielding $A_{0+}^{(2)}(\text{app}) = -0.83 \pm 0.06$ and $A_{0+}^{(4)}(\text{app}) = +0.25 \pm 0.03$.

distribution where the quantization axis \hat{z} lies along the surface normal. $A_{0+}^{(2)}$ and $A_{0+}^{(4)}$ are related to the expectation values of the angular momentum operators

$$A_{0+}^{(2)} = \langle (J_i | (3J_z^2 - J^2) / J^2 | J_i) \rangle \quad (4a)$$

and

$$A_{0+}^{(4)} = (1/8) \langle (J_i | (3J^4 - 6J^2 - 30J_z^2 J^2 + 25J_z^2 + 35J_z^4) / (J^4) | J_i) \rangle. \quad (4b)$$

The moments of the line strength are, in general, dependent on the rotational quantum numbers and electronic symmetry of the levels involved as well as on the laser polarization and the experimental geometry. A detailed discussion of the calculation and interpretation of the $P_{q+}^{(k)}$ moments is given elsewhere²⁵; for the present analysis the $P_{q+}^{(k)}$ are simply numbers which are readily calculated for a given transition and laser polarization.

Experimentally, the degree of polarization for a particular rotational level is determined by recording the intensity of a transition originating from that level while varying the direction of polarization of the laser with respect to the surface normal. An example of this type of measurement is shown in Fig. 3(a) for the $J = 15$ line of the O branch, denoted as $O(15)$, and in Fig. 3(b) for the $P(15)$ line. Note the difference in the waveforms for the two branches shown in Fig. 3 remembering that the two transitions probe the same

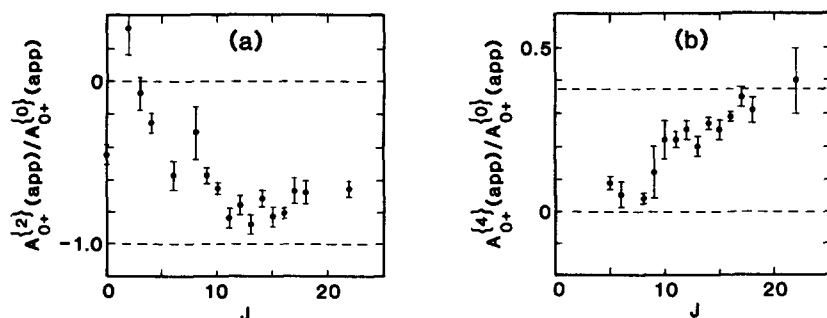


FIG. 4. Quadrupole [$A_{0+}^{(2)}(\text{app})$] and hexadecapole [$A_{0+}^{(4)}(\text{app})$] alignment moments as a function of rotational quantum number J for $E_i = 0.3$ eV, $\theta_i = 15^\circ$, $\theta_f = 20^\circ$, and $T_s = 90$ K.

ground state level. The strong variation in intensity with laser polarization and rotational branch illustrates the necessity for understanding the polarization of the sample in order to extract reliable rotational state populations. The data are acquired in the form of multiple wavelength scans across a given spectral feature in which the polarization of the laser is changed between scans. The integrated area under the peak is then used in subsequent analysis.

For two-photon excitation, it is insufficient to record the transition intensity at only two polarization settings because three (or more if the assumption of cylindrical symmetry is not valid) terms may contribute to Eq. (3).²⁵ Our procedure is to measure the intensity of a particular transition at twelve polarization angles and then perform a least-squares fit of the data to Eq. (3) to determine $A_{0+}^{(2)}$ and $A_{0+}^{(4)}$. By overdetermining the system we can obtain a meaningful error analysis and also check the validity of Eq. (3). When two rotational branches are measured, as in Fig. 3, the data from both are jointly fit. The solid curves in Fig. 3 are fits, yielding $A_{0+}^{(2)}(J=15) = -0.83 \pm 0.06$ and $A_{0+}^{(4)}(J=15) = +0.25 \pm 0.03$; the errors are one standard deviation and are determined from the fitting routine. The quality of the fits indicates that the three terms included in Eq. (3) are sufficient to describe the data. The significance of the values of these moments is discussed below. The effect of a possible deviation from our assumption of cylindrical symmetry

[which could add additional terms or change the identification of the terms in Eq. (3)] is discussed in the Appendix.

We record data like that shown in Fig. 3 for each well resolved line in a spectrum, such as Fig. 2(b), to determine the $A_{0+}^{(2)}$ and $A_{0+}^{(4)}$ alignment moments for each rotational level. Figure 4 shows the results as a function of rotational quantum number for an incident beam energy of 0.3 eV, an incident angle of 15° , and a surface temperature of $T_s = 90$ K. For $J < 4$, there are no transitions for which the lines are not overlapped with other transitions, usually originating from higher rotational levels. However, knowledge of the polarization behavior of the higher rotational level (i.e., from data like Fig. 3) and the relative intensities of the blended and unblended lines at one polarization [i.e., from Fig. 2(b)] permit us to deconvolve the data on a point-by-point basis. This procedure works well on lines where the high J transition contributes a small (<20%) part of the intensity to the blended line. The error bars for $J > 3$ in Fig. 4 are simply determined from the statistics of the fit; for $J \leq 3$, the errors associated with knowing the $A_{0+}^{(0)}$, $A_{0+}^{(2)}$, and $A_{0+}^{(4)}$ for the blended line are also included in the error estimate for the fitted line. The redundancy of multiple measurements of $A_{0+}^{(2)}$ and $A_{0+}^{(4)}$ provided by probing different rotational branches serves as an additional consistency check on our results.

Figure 5 shows how the alignment varies with incident

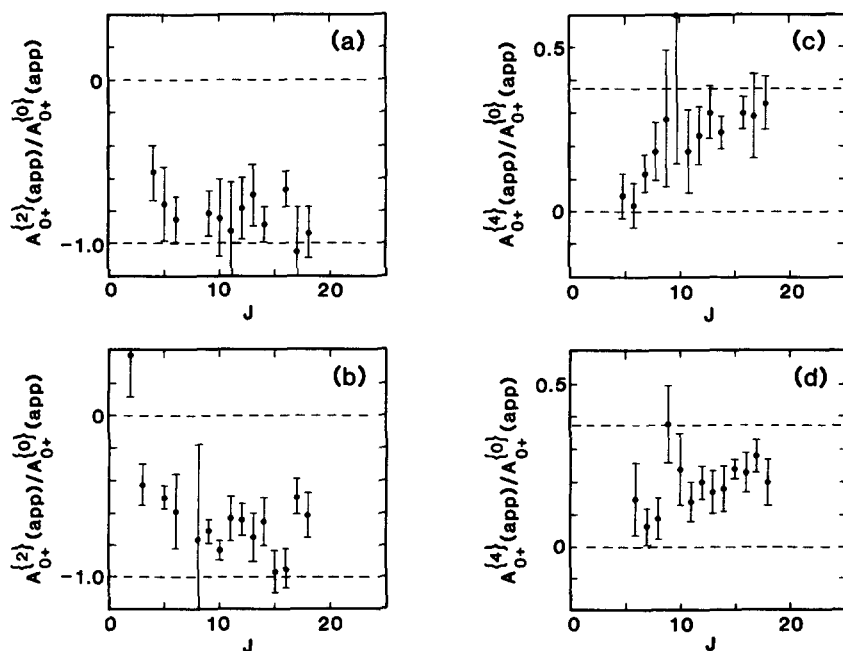


FIG. 5. Alignment moments vs J for $E_i = 0.2$ eV, $T_s = 390$ K, and (a) $\theta_i = 15^\circ$, $\theta_f = 20^\circ$ and (b) $\theta_i = 45^\circ$, $\theta_f = 45^\circ$.

angle. The data are for $E_i = 0.2$ eV, $T_s = 390$ K, $\theta_i = 15^\circ$, and $\theta_f = 45^\circ$. It is clear that essentially no difference is observed within the error bars. Comparison of Figs. 4 and 5 (as well as other data taken at $E_i = 0.1$ and 0.4 eV) also shows that changes in T_s and E_i do not cause any significant change in the alignment at the specular angle.

2. Interpretation

The observation of nonzero values for the $A_{0+}^{(2)}$ and $A_{0+}^{(4)}$ moments indicates that the angular momentum of the scattered N₂ is aligned with respect to the surface normal. A negative sign for the quadrupole moment $A_{0+}^{(2)}$ implies that the scattered N₂ is preferentially rotating with \mathbf{J} lying in the plane of the surface, corresponding to excess population of states with low $|M_z|$ values. In the present case $M_z = \langle J_z \rangle$, i.e., M_z is the projection of \mathbf{J} onto the z axis which is taken to be along the surface normal. The hexadecapole moment $A_{0+}^{(4)}$, being roughly a measure of $\langle \cos^4 \theta \rangle$ where θ is the angle between \mathbf{J} and $\hat{\mathbf{n}}$, is useful for describing more extreme distributions. Interpretation of the $A_{0+}^{(4)}$ moment requires prior knowledge of the $A_{0+}^{(2)}$ value since $A_{0+}^{(4)}$ can be positive if \mathbf{J} is along $\hat{\mathbf{n}}$ or if \mathbf{J} is perpendicular to $\hat{\mathbf{n}}$. The limiting values for the quadrupole moment are $A_{0+}^{(2)} = +2.0$ for \mathbf{J} parallel to $\hat{\mathbf{n}}$ and $A_{0+}^{(2)} = -1.0$ for \mathbf{J} perpendicular to $\hat{\mathbf{n}}$. The extreme values for the hexadecapole moment at high J are $A_{0+}^{(4)} = 0.75$ for \mathbf{J} parallel to $\hat{\mathbf{n}}$, $A_{0+}^{(4)} = -0.5$ for \mathbf{J} at 49° with respect to $\hat{\mathbf{n}}$, and $A_{0+}^{(4)} = 0.375$ for \mathbf{J} perpendicular to $\hat{\mathbf{n}}$. From our observation of negative $A_{0+}^{(2)}$ we deduce that \mathbf{J} lies perpendicular to $\hat{\mathbf{n}}$, and the values $A_{0+}^{(4)}$ derived from the data reinforce this conclusion.

It is easy to see how polarization may be produced in gas-surface scattering. The forces acting on the gas molecule during the collision with the surface are clearly not isotropic but are directed predominantly along the surface normal. If these forces torque the molecule to excite rotation, then the rotation will be polarized with the plane of rotation perpendicular to the surface, i.e., the molecule will tend to rotate with its angular momentum vector \mathbf{J} parallel to the plane of the surface. This type of motion has been termed "cartwheeling" and rotation with $\mathbf{J} \parallel \hat{\mathbf{n}}$ is labeled "helicoptering."^{13,31}

The data in Figs. 4 and 5 show near zero polarization at $1 < J < 3$, a monotonic increase in polarization at intermediate J , which smoothly approaches the limiting polarization values for \mathbf{J} perpendicular to $\hat{\mathbf{n}}$ at high J . We do not observe a large decrease in polarization at the highest J , as was reported for NO/Ag(111).^{9,10} In some cases, we observe a positive quadrupole alignment at low J , in particular for $J = 2$ as shown in Figs. 4 and 5. This may be the result of a dynamical bias in the scattering of the kind suggested by Lauderdale, McNutt, and McCurdy.³² In this model, incident molecules in $J = 2$ with $\mathbf{J} \perp \hat{\mathbf{n}}$ (i.e., undergoing a cartwheeling-type motion) are more likely to be excited to higher J . Those molecules with $\mathbf{J} \parallel \hat{\mathbf{n}}$ (i.e., helicoptering) have a greater probability of being elastically scattered with $J = 2$, thus yielding a positive contribution to the $A_{0+}^{(2)}$ moment.

The measured alignment is useful for a qualitative understanding of the scattering process, but perhaps the most

important information comes from direct comparison with model calculations. Lauderdale *et al.*³² carried out quantum calculations using both close-coupling methods and the sudden approximation to study polarization effects in diatom-surface collisions. They conclude that small ΔM transition probabilities are primarily responsible for polarizing the molecule. Furthermore, they state that dynamical bias in the scattering is important but may be difficult to observe. Their model did not include surface corrugation. Corey and Alexander³³ have studied the scattering of N₂ from model Ag surfaces using the quantum close-coupled techniques that they had previously applied to the NO/Ag(111) system.³⁴ They were able to include surface corrugation and study alignment effects, because of the fourfold reduction in the number of channels needed for N₂ vs NO (since no fine structure or Λ -doublet states had to be considered). Their initial conditions simulated those of this study. For an uncorrugated surface, they found a more rapid increase in alignment with J than we observe experimentally (see Fig. 3 of Ref. 32 for this comparison). On the (111) surface, the effect of increasing the corrugation was to add structure in the alignment (specifically a decrease in alignment around $J = 6$) because of $\Delta M = \pm 6$ selection rules arising from the lattice symmetry.

The lack of large alignment observed at $J < 10$ is not entirely the result of the nonzero population of states with $J > 0$ in the incident beam (and the concurrent isotropic M state distribution); Fig. 3 of the paper by Corey and Alexander³³ illustrates this point. The discrepancy may be one of the most important results of the present work and indicates that the flat surface approximation is not valid; i.e., there must be forces in the plane of the surface which serve to reduce the observed alignment. The fact that the higher rotational levels are almost completely aligned is expected even for a corrugated surface. As pointed out by Lauderdale *et al.*,³² in order to scatter into a high J state, the molecule must effectively hit the top of the bump on the surface. Therefore, the impulse is still directed along $\hat{\mathbf{n}}$. Our orientation results³⁰ also indicate the importance of in-plane forces in the scattering.

Wolf, Collins, and Mayne³⁵ performed classical calculations for a rigid rotor-rigid surface model and determined b_2/b_0 (which is proportional to $A_{0+}^{(2)}$) for model potentials with different amounts of corrugation. Their calculations were for a lattice with rectangular symmetry [Ag(111) has hexagonal symmetry]; Corey and Alexander³³ found that the lattice symmetry had a strong effect on the alignment. Qualitatively, the results of Wolf *et al.* look similar to our data; the closest agreement is with the results calculated for low surface corrugation, as might be expected for Ag(111). In a subsequent paper Wolf *et al.*³¹ calculated the population, as well as the $A_{0+}^{(2)}$ and $A_{0+}^{(4)}$ alignment moments, while varying the steepness of the repulsive potential, the corrugation of the surface, and the incident translational energy. For more corrugated surfaces and/or higher energy, their results also show structure in the alignment moments vs J , similar to that reported by Corey and Alexander.³³ The possibility of observing such features on a rougher surface is intriguing and worth further study. We do not find such

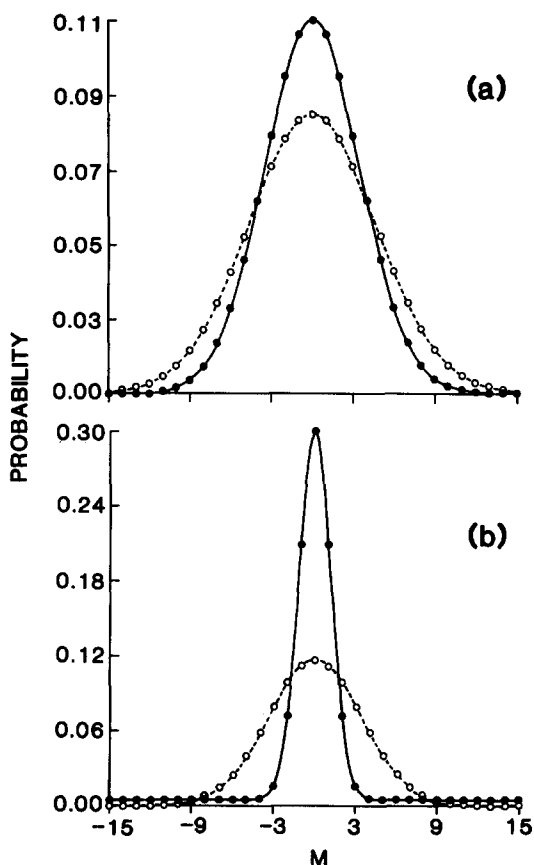


FIG. 6. Model M state probability distributions for $J=15$. In (a) $P(M) = C \exp(-\alpha M^2)$ and in (b) $P(M) = C \exp(-\beta M^2) + \text{constant}$. See the text for the values of the constants used. In both (a) and (b) the solid curve describes the data of Fig. 3 better.

structure; it might be masked experimentally by the surface motion (which is absent in the calculations). It is interesting to note that the GLE calculations of Tully and co-workers for NO/Ag(111)¹ which do include surface motion and corrugation, do not show the structure in the $A_{0+}^{(2)}$ alignment moment seen in the quantum mechanical calculations.

The two higher order moments measured do not completely determine the spatial distribution of \mathbf{J} , so it is appropriate at this point to illustrate what information they do contain. To do this, we plot in Fig. 6 several model distributions and give the moments calculated from them according to Eq. (4a) and Eq. (4b). It should be emphasized that these distributions are by no means unique but are meant to illustrate possible forms the distribution could take. We follow this procedure rather than just summing the three terms of Eq. (1) for which we have direct measurement because the observed values of $A_{0+}^{(2)}$ and $A_{0+}^{(4)}$ at high J are close enough to their perfect alignment limits so that the expansion in Eq. (1) necessarily has higher order terms that are nonzero. Indeed, if we were to obtain $A_{0+}^{(2)} = -1$ with no uncertainty, there would be only one distribution consistent with this, i.e., all population in $M = 0$ and all higher order terms would be fixed (i.e., $A_{0+}^{(4)} = +0.375$, $A_{0+}^{(6)} = \text{constant} \neq 0$, etc.). This point is discussed more fully elsewhere.³⁶

The model used in Fig. 6(a) assumes a distribution of the form

$$P(M) = C \cdot \exp(-\alpha M^2), \quad (5)$$

where $P(M)$ is the probability of being in the state M , α is an adjustable parameter, and C is a normalization constant. The plot is for $J = 15$, and a value of $\alpha = 0.225$ gives approximately the observed $A_{0+}^{(2)}$ and $A_{0+}^{(4)}$ values of $A_{0+}^{(2)} = -0.85$ and $A_{0+}^{(4)} = 0.22$. Changing the width parameter α to 0.30 gives a wider M distribution and correspondingly smaller values of the alignments ($A_{0+}^{(2)} = -0.73$ and $A_{0+}^{(4)} = +0.14$). Figure 6(b) illustrates the additional information gained by measuring the $A_{0+}^{(4)}$ moment. We plot two different distributions that yield the same $A_{0+}^{(2)}$ moment but different values for $A_{0+}^{(4)}$. The solid curve uses Eq. (5) with $\alpha = 0.220$ (yielding $A_{0+}^{(2)} = -0.86$ and $A_{0+}^{(4)} = +0.22$); the dashed curve uses

$$P(M) = C [\exp(-\alpha M^2) + c] \quad (6)$$

with $\alpha = 0.075$ and $c = 0.015$ yielding $A_{0+}^{(2)} = -0.85$ and $A_{0+}^{(4)} = +0.30$. Both curves are normalized to unity. The observed $A_{0+}^{(4)}$ value of $+0.25$ favors the solid curve and shows the utility of the higher order $A_{0+}^{(4)}$ term in describing more skewed distributions.

The discussion above does not exclude a distribution with M rainbows arising from ΔM propensity rules related to the azimuthal symmetry of the lattice as predicted by quantum and semiclassical models of the scattering.^{2,33} In fact, many distributions consistent with the observed alignment can be readily constructed; we are simply trying to convey a feel for the meaning of the values of the measured alignment moments.

Based on the relative rotational state populations (given below) and the alignment moments just presented, we can calculate an overall quadrupole alignment by performing a weighted average:

$$\langle A_{0+}^{(2)} \rangle = \sum_J [a_{0+}^{(0)}(J)] A_{0+}^{(2)}(J) / \sum_J [a_{0+}^{(0)}(J)].$$

Evaluating this expression for the conditions of Fig. 4 yields $\langle A_{0+}^{(2)} \rangle = -0.75$ at specular. Thus, a sizeable overall alignment is found for the scattered beam.

C. Time-of-flight measurements

Most laser based detection techniques (including the two-photon excitation scheme presently employed) are sensitive to density; the quantities usually of interest are flux weighted because of their connection to cross sections. Conversion between the two requires knowledge of the velocity distribution. Experimentally, a time-of-flight distribution is obtained by scanning the delay between the chopper opening and the laser firing while monitoring the ion intensity with the laser wavelength tuned to a transition. We have performed a series of measurements at normal incidence with $\theta_i = \theta_f = 0^\circ$. Calibration of the surface-to-ionizer distance is readily achieved by translating the crystal a known distance along the molecular beam direction and measuring the change in the arrival time of the scattered beam. After subtracting the extra time required for the incident beam to reach the crystal, this procedure gives directly the average velocity of the specularly scattered beam. Note that no assumptions are needed about the residence time. This proce-

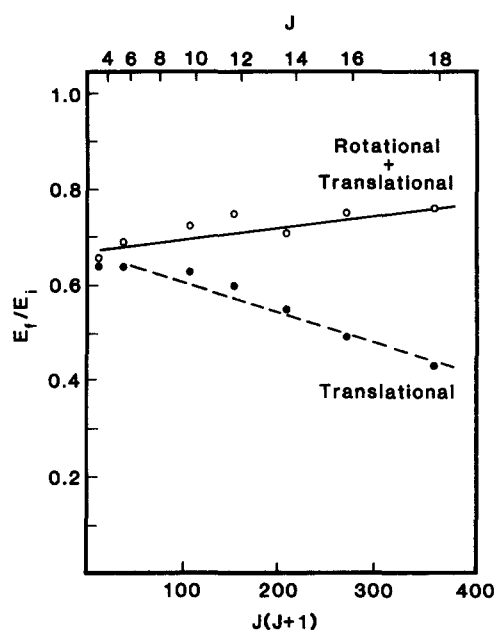


FIG. 7. Scattered N_2 energy distributions as a function of rotational energy: the solid symbols are translational energy and the open ones are total (translational plus rotational) energy.

ture assumes that there is no strong correlation between velocity and final angle; this correlation is known to be weak for $NO/Ag(111)$.³⁷

Results are shown in Fig. 7 for an incident energy of 0.3 eV and a surface temperature of 90 K. The crystal-to-ionizer distance was set to 2.6 cm for these measurements. Plotted are the final (average) translational energy and the total internal energy (translational plus rotational) vs $J(J+1)$. Both final energies are scaled to the incident energy. The data show a strong correlation between final rotation and translation in which higher rotational excitation pairs up with lower translational energy. The results also show that the molecule loses 20%–30% of its incident energy to the solid and that this percentage decreases with J . This trend with J has been reported previously for the $NO/Ag(111)$ system³⁷ and for the NO/Ge system.³⁸ This was attributed to the molecule's lower effective mass (and hence less efficient energy transfer to the solid) for those orientations leading to high rotational excitation. Our results support this interpretation.

The 20%–30% energy loss to the surface is typical of what has been seen for scattering of heavy particles under similar conditions, such as $N_2/Pt(111)$ ³⁹ and $NO/Ag(111)$.³⁷ For NO/Ge the energy loss to the surface is as much as 57%.³⁸ Within the hard cube model, the energy transfer is governed by the ratio of the mass of the molecule to the effective surface mass and ellipse (molecule) orientation. For the observed energy loss, the effective surface mass is approximately ten times the N_2 mass. This corresponds to about 2.5 times the mass of a silver atom and qualitatively indicates that the N_2 interacts with several surface atoms.

In Sec. III D we discuss how our average velocity results affect the determination of relative population distributions; here we comment on how they relate to the alignment. If the

degree of alignment is correlated with velocity, then the measurements shown in Figs. 4 and 5 will be an average over the velocity distribution weighted in favor of the slower moving component of the scattered beam. We have investigated this possibility in two ways. First, we measure TOF curves for orthogonal settings of the laser polarization. In this procedure, for the O branch, $E\parallel\hat{n}$ probes preferentially states with $M=0$ whereas $E\perp\hat{n}$ probes states with $M=\pm J$. Second, we set the time delay to the peak or the wings of the TOF distribution and recorded alignment data such as that of Fig. 3. In both cases no difference was observed for either low J ($J=4$) or high J ($J=12$ or 14). Velocity differences on the order of $\Delta v/v=0.05$ can be readily observed. Therefore, we conclude that any correlation between velocity and alignment is weak (at a fixed exit angle) and that the moments presented in Figs. 4 and 5 are equivalent to the true flux weighted alignment as a function of J .

D. Rotational population

Once the alignment is known for each J value, then the relative population $a_{0+}^{(0)}(J)$ can be extracted by analyzing a REMPI spectrum [such as Fig. 2(b)] using Eq. (3). We do not have complete sets of alignment data for all the surface temperatures, incident angles, and incident energies for which we have complete scans of the type shown in Fig. 2(b). Instead we use a functional form fitted to data of the kind shown in Figs. 4 and 5 to supply the alignment moments not measured but needed to determine the relative values of $a_{0+}^{(0)}(J)$. This procedure is reasonable based on the small variation of the alignment with T_s and E_i as well as on the smooth variation of alignment with J . Measurements of selected lines at various T_s and E_i confirm that the alignment varies little with these parameters. Using this procedure, it is found that the $a_{0+}^{(0)}$ values derived from different rotational branches agree across the range of J values studied.

Results are shown in Fig. 8 for the conditions: $E_i=0.3$ eV, $\theta_i=15^\circ$, $\theta_f=20^\circ$, and $T_s=90$ K. The data are presented in the form of a Boltzmann plot, i.e., a plot of $\ln\{a_{0+}^{(0)}/[(2J+1)g_r(J)]\}$ vs $J(J+1)$, where $(2J+1)$ is the rotational state degeneracy, $g_r(J)$ is the nuclear spin state degeneracy, and $J(J+1)$ is proportional to the rotational energy. If the distribution were described by a temperature, the data would lie on a straight line. For experiments performed on isotropic background gas (admitted to the chamber through a leak valve), this is the case, and a least squares fit yields $T=300\pm 10$ K. Also shown in Fig. 8 are the same data, corrected for the J -dependent average velocity, assuming the results of Fig. 7 (taken at $\theta_i=\theta_f=0^\circ$) are applicable at $\theta_i=15^\circ$ and $\theta_f=20^\circ$. The $a_{0+}^{(0)}$ moments are multiplied by the factor $v(J)/v_{\max}$ for each J where $v(J)$ is determined from a least-squares fit to a straight line of the data of Fig. 7, and v_{\max} is the maximum velocity, as determined from the maximum value of the final translational energy in Fig. 6. This correction makes very little difference in the Boltzmann plot.

Figure 9 shows the change of the population distribution with incident energy for $\theta_i=15^\circ$, $\theta_f=20^\circ$, and $T_s=90$

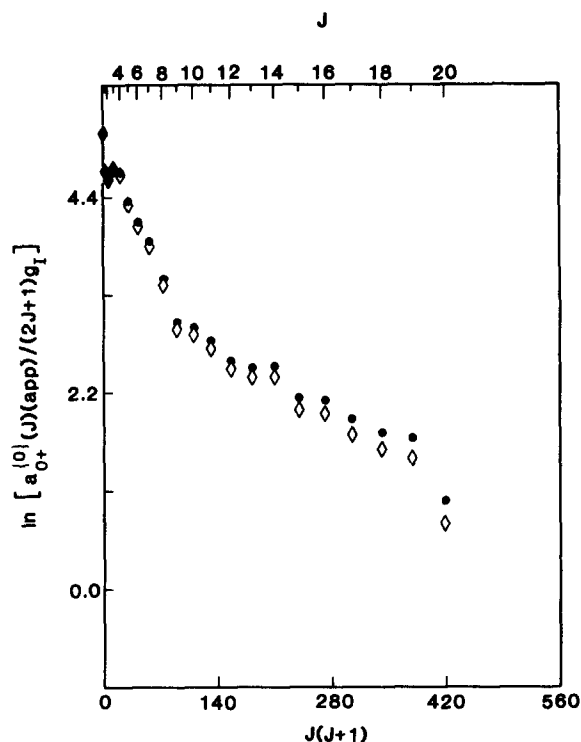


FIG. 8. Rotational state distributions of N₂ scattered off Ag(111) for the conditions of Figs. 2 and 4. Plotted is the logarithm of the population divided by the rotational and nuclear spin degeneracies vs $J(J+1)$. The solid circles are the uncorrected data; the open diamonds are corrected for a density-flux transformation using the data from Fig. 7.

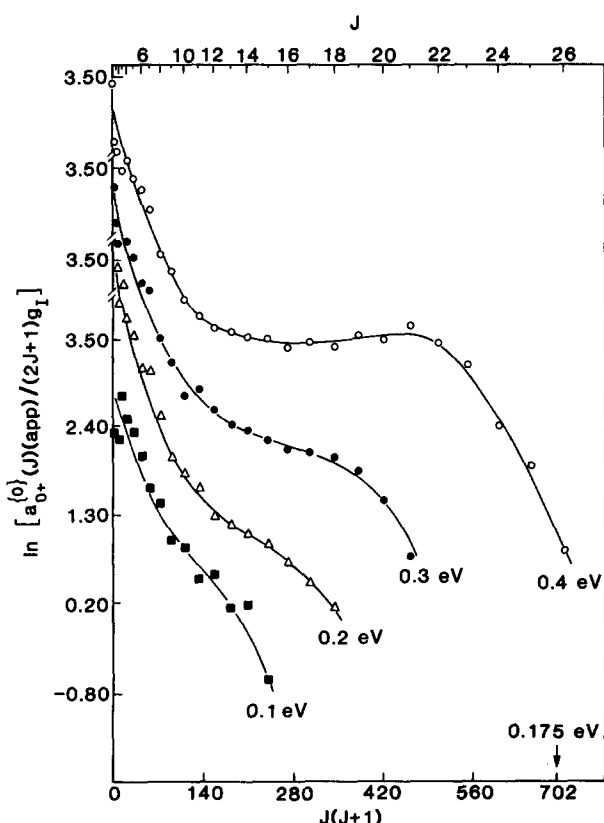


FIG. 9. Boltzmann population plots as a function of incident beam energy for $\theta_i = 15^\circ$, $\theta_f = 20^\circ$, and $T_s = 90$ K.

K. The final angle θ_f corresponds approximately to the peak of the scattered intensity. (As a measure of the total intensity at a given angle we use $\sum_j \{a_{0+}^{(0)}(J)\}$.) These data are not corrected for any ν - J correlation of the type shown in Fig. 7. For higher values of the incident energy, the distributions are not well described by a temperature but show a broad region of excess population at high J . Similar trends were obtained for NO/Ag(111)^{7,11} and were interpreted as rotational rainbows. Classically, the rainbow arises from an extremum in the excitation function as a function of the rotor orientation.³⁹ The data of Fig. 8 support this interpretation because the position of the rainbow shifts to higher J as the collision energy is increased.

In addition to observing a strong dependence of the rotational populations on incident energy, we see a striking variation with final scattering angle. The results are shown in Fig. 10 for $\theta_i = 30^\circ$, $E_i = 0.3$ eV, and $T_s = 90$ K. The data in Fig. 10(a) correspond to the angle of maximum total intensity ($\theta_f \sim 35^\circ$); the data in Fig. 10(b) were taken at $\theta_f \sim 50^\circ$ (superspecular); and the data in Fig. 10(c) at $\theta_f \sim 25^\circ$ (subspecular). The curves are scaled relative to one another so the populations are directly comparable. This assumes that our ion collection efficiency does not vary appreciably in this angular range. The alignment as a function of exit angle does not change substantially and will be presented together with orientation results.³⁰ The population data show that at more grazing exit angles (further from the surface normal), substantially greater population is shifted to higher J levels. This result agrees qualitatively with simple one-dimensional scattering models in which only linear momentum normal to the surface is coupled to rotation and the parallel component of the linear momentum is conserved. Thus highly rotationally excited products exit further from \hat{n} .

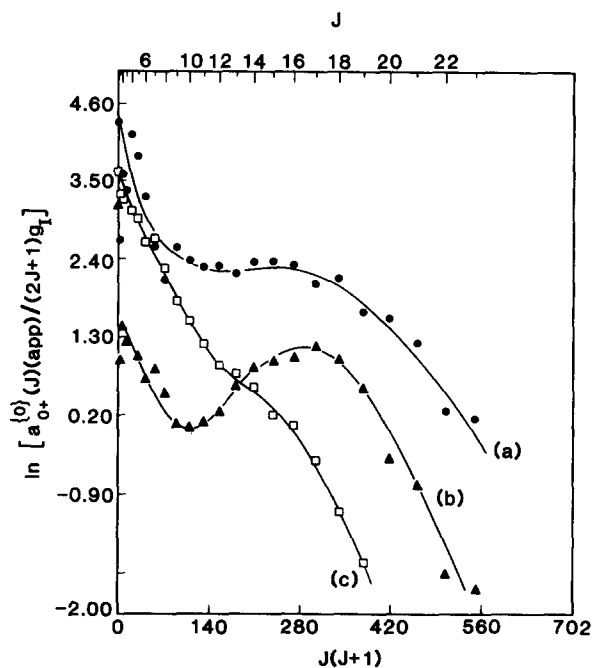


FIG. 10. Boltzmann population plots as a function of final scattering angle for $\theta_i = 30^\circ$, $E_i = 0.3$ eV, and $T_s = 90$ K. Final angles are (a) $\theta_f = 35^\circ$, (b) $\theta_f = 50^\circ$, and (c) $\theta_f = 25^\circ$.

Asada and Matsui¹⁷ showed that for N₂ scattering from Ag(111) at $E_i = 0.09$ eV, $\theta_i = 50^\circ$, and $T_s = 500$ K, the mean speed for the scattered N₂ varies by approximately 20% with final scattering angle. Assuming an effect of the same magnitude for our conditions, this would change the relative scaling factors between plots (a), (b), and (c) in Fig. 10. Figure 10(b) would be shifted down by $-\ln(0.9) = -0.1$ and Fig. 10(c) up by ~ 0.1 . This would cause only a minor change in the plot. Asada and Matsui¹⁷ also showed that the width of the speed distribution is relatively constant as a function of final scattering angle. Therefore, it is unlikely that the variation in the population distribution with J and θ_f shown in Fig. 10 is a result of a radically different form of the translational energy distribution as a function of J at the different final scattering angles.

The dramatic variation of the population distribution with θ_f at low T_s is largely smeared out as the surface temperature is raised. Results are shown in Fig. 11 for the same conditions as in Fig. 10 except that $T_s = 520$ K. The final angle must be scanned further from the intensity peak in order to observe a significant change in the distributions as evidenced by the substantially lower intensity of Fig. 11(b) relative to Fig. 11(a). This behavior is most likely caused by either an increase in the microscopic surface roughness or by greater participation of phonons at high T_s ; both possibilities would blur the correlation between J and θ_f .

Asada¹⁶ reported a slight shift (toward \hat{n}) and broadening of the overall angular distribution with increasing surface temperature for N₂/Ag(111) although T_s was varied only from 500 to 600 K. Subsequently, Asada and Matsui¹⁷ showed that at $T_s = 500$ K the average speed is a strong function of final angle, but they did not discuss how a change in T_s affects this quantity. For direct scattering of N₂ from

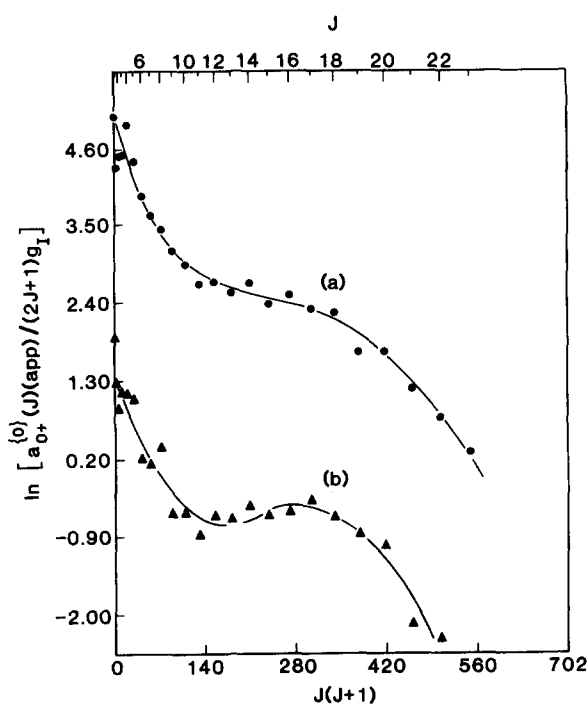


FIG. 11. Boltzmann population plots as a function of final scattering angle for $\theta_i = 30^\circ$, $E_i = 0.3$ eV, and $T_s = 520$ K. Final angles are (a) $\theta_f = 35^\circ$ and (b) $\theta_f = 55^\circ$.

Pt(111), Janda *et al.*³⁹ also found a strong variation of velocity with angle, and this feature persisted even at high T_s (900 K); their results for N₂³⁹ and Ar⁴⁰ were very similar, indicating a lack of participation by the rotational degree of freedom of the N₂. Our results show that angle-resolved rotational distributions are sensitive to some feature of the surface that depends on temperature, but this feature does not greatly affect the velocity and nonrotational state resolved angular distributions of the scattered N₂.

Our results are similar to the scattering of HD from Pt(111)⁴¹ where it was observed that the $\Delta J = 1$ and 2 peaks are smeared out in final angle as T_s is raised from 500 to 900 K. However, this effect has not been seen before for molecules heavier than D₂. The rotational state distributions for NO/Ir(111)⁴² are reported to vary with final angle, but this difference arises from a change in the scattering mechanism from trapping/desorption to direct inelastic. KLA⁸ and later Rettner *et al.*³⁷ reported rotational state resolved angular distributions for NO/Ag(111) for selected J levels; they observed that for higher rotational levels the angular distribution peaks further from the normal. They did not present data on how changes in the surface temperature may affect their results.

When looking at the final angle of maximum intensity (i.e., the quasispecular angle) for incident beam energies greater than 0.1 eV, we see essentially no change in the rotational state distributions as the surface temperature is varied in the range of 90–700 K. This indicates that the surface does not play an active role in determining the overall amount of rotational excitation for these beam energies.

Corey and Alexander,³³ using the close-coupled calculations mentioned earlier, were able to qualitatively reproduce the measured rotational state distributions for N₂/Ag(111). They used a modified form of the potential which was used by Muhlhausen *et al.*^{15,18} in modeling the velocity and angular results for N₂/Ag(100). The primary change in the potential was an increase in the anisotropy of the repulsive wall with respect to the orientation geometry of the N₂ internuclear axis. The potential of Muhlhausen *et al.* was found by Corey and Alexander to underestimate substantially the rotational inelasticity. The agreement with experiment was not quantitative; again the most likely explanation is the role of surface motion in the overall energy transfer.

E. Comparison to NO/Ag(111) results

1. Alignment

For the well studied NO/Ag(111) system KLA^{9,10} determined b_2/b_0 where b_i is the i th term in a Legendre expansion of the spatial J distribution. According to their normalization b_2/b_0 would equal -2.5 for J perfectly aligned perpendicular to \hat{n} ($M = 0$); they observed low polarization for $J < 10.5$, increasing with J in the range $10.5 < J < 25.5$ to a maximum of $b_2/b_0 = -1.75$, then decreasing back to zero for $J > 40.5$. They also observed that the maximum amount of alignment decreases as the incident angle is increased, a result that we do not see for N₂.

Our results show a faster falloff with J and a maximum alignment closer to the perfect alignment limit. Perhaps

most interesting, we do not observe the strong depolarization at very high J reported by KLA. In some cases, we find a significant decrease ($\sim 20\%$) in the alignment at high J ; this decrease is usually associated with measuring a large orientation for the J in question. We will present these results in detail elsewhere,³⁰ but we suggest that the apparent decrease in alignment seen by KLA may be caused by a breakdown in the assumption of cylindrical symmetry. Further discussion of the possible effects of noncylindrical symmetry is presented in the Appendix.

2. Populations

The shape of the relative population distributions and the variation with incident energy for N₂ and for NO scattered from Ag(111) are both very similar. The primary difference is in the extent of rotational excitation. In Fig. 12 we plot our results for $E_i = 0.2$ eV, $\theta_i = 15^\circ$ ($E_n = 2100$ K), $\theta_f = 20^\circ$, and the results of Kubiak *et al.*¹¹ at $E_n = 2321$ K (0.2 eV, $\theta_i = 0^\circ$). Both data sets are for $T_s = 475$ K. The difference in the degree of rotational inelasticity is the most interesting aspect of this figure; for NO, rotational excitation occurs to $N = 36$, while for N₂, the distribution extends only to $J = 20$. Kubiak *et al.* report for NO an average rotational energy of 537 K for $\Omega = 1/2$ and $\langle E_r \rangle = 632$ K for $\Omega = 3/2$, whereas we calculate for N₂,

$$\langle E_r \rangle = \sum \{a_0^{(0)}(J)BJ(J+1)\} / \sum \{a_0^{(0)}(J)\} = 226 \text{ K}$$

under similar conditions.

Several features of the potential may contribute to this difference. The molecule actually hits the repulsive wall of the potential with the incident energy plus the energy gained in passing over the attractive well. We can estimate the effect that a difference in the well depths would have on the rotational excitation based on NO/Ag(111) results. Kubiak *et al.*¹¹ were able to fit their data to a bilinear equation, where the average amount of energy transferred into rotation $\langle E_r \rangle$ varied linearly with both the normal kinetic energy $\langle E_n \rangle$ and with the surface temperature T_s . An additional constant

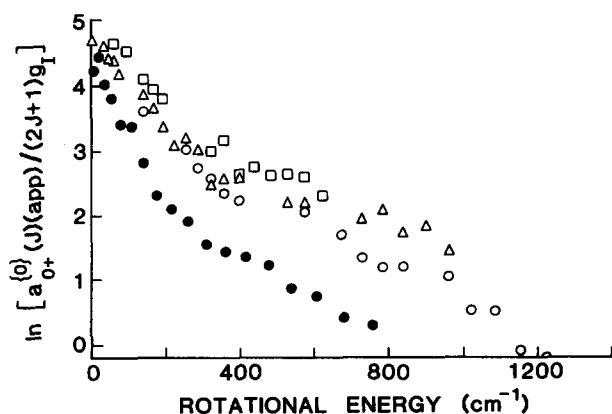


FIG. 12. Comparison of Boltzmann population plots for N₂ (solid circles) and NO (open symbols) scattered off Ag(111) under similar conditions. The N₂ data is ours; the NO results are from Kubiak *et al.* (Ref. 10). Different symbols for NO are for different rotational branches of the $\Omega = 1/2$ fine structure state: circles are $Q(1)$, triangles are $R(1)$, and the squares are for $S(1)$.

term, independent of both E_n and T_s , appeared in the formula and was interpreted as a measure of the depth of the NO-Ag(111) attractive well. The depth of the well for NO/Ag(111) is generally accepted to be about 0.2 eV.¹¹ This should be compared with the estimate of Muhlhausen *et al.*¹⁸ for N₂/Ag(111) of 0.1 eV. Thus, the difference in well depths is estimated to be about 0.1 eV. Based on the bilinear fit of Kubiak *et al.*,¹¹ this 0.1 eV difference contributes $(0.088)(2850 \text{ K})(1/2) = 125 \text{ K}$ for $\Omega = 1/2$ and $(0.132)(2080 \text{ K})(1/2) = 137 \text{ K}$ for $\Omega = 3/2$ to $\langle E_r \rangle$. Thus, if the NO/Ag(111) well depth were only half the actual value, the average rotational energy would be approximately 500 K for $\Omega = 1/2$ and 400 K for $\Omega = 3/2$, which is still significantly greater than that observed for N₂. Therefore, it seems that the difference in the depth of the wells cannot account completely for the difference in rotational inelasticity.

At least three other factors could also contribute to the difference: (1) an orientational anisotropy in the attractive part of the NO/Ag(111) potential, i.e., a preference for the "N" end vs the "O" end of the molecule would apply a torque to the molecule that could increase the rotational inelasticity of NO relative to N₂. Trajectory calculations for NO/Ag(111)¹ show that this feature plays a large role in the rotational inelasticity; (2) a difference in the anisotropy of the repulsive wall of the potential for NO vs N₂ would have the same effect. However, the calculations of Wolf *et al.*^{31,35} show that a more anisotropic repulsive potential should give higher alignment, not lower, as observed for NO vs N₂; and (3) the offset of the center of mass from the geometric center of the molecule for NO could also increase the inelasticity, although for NO this effect should be small. Within the hard cube model this results in less than a 10% change in the rotational inelasticity. Thus, the evidence appears to point to greater anisotropy in the attractive part of the NO/Ag(111) potential as accounting for the greater rotational inelasticity of NO vs N₂.

IV. CONCLUSIONS

The internal state distributions resulting from scattering of an initially rotationally cold beam of N₂ from a clean Ag(111) surface have been studied using resonance enhanced multiphoton ionization. The population, quadrupole, and hexadecapole moments of the alignment have been determined as a function of rotational quantum number.

The goal of molecular beam experiments is to define the initial conditions as well (and as narrowly) as possible and to measure the final distributions to the highest level of detail. The present results represent a step in this direction and, together with our orientation results,³⁰ provide a more stringent test of the potentials used to model N₂/Ag(111) gas-surface scattering.

The scattering is confirmed to be direct, based on strong variations in the rotational state populations with incident energy. The rotational state populations show pronounced rainbow structure at higher incident energy and/or more glancing exit angles. A strong variation is also observed as a function of final scattering angle at low surface temperature; the magnitude of the effect decreases at higher T_s . The N₂

rotational state distributions at the angle corresponding to the maximum total intensity are found to be insensitive to T_s .

Time-of-flight measurements have been analyzed to yield average translational energies as a function of rotational level. A strong correlation is observed with higher rotationally excited molecules having lower translational energy. However, higher rotational levels are seen to leave the surface with greater total energy.

The scattered N₂ is found to be highly aligned with \mathbf{J} lying in a plane parallel to the surface, although the degree of alignment at intermediate J (J of 3–8) is less than that expected for a flat surface. At high J the alignment approaches the limiting value for \mathbf{J} being perpendicular to the surface normal. The alignment at specular is not sensitive to incident particle energy in the range of 0.1–0.4 eV or surface temperature in the range of 90–520 K. No correlations were found between alignment and velocity.

ACKNOWLEDGMENTS

The assistance of Melissa Hines is gratefully acknowledged. This work was supported by the Office of Naval Research under Grant No. N00014-87-K-0265.

APPENDIX

As stated earlier, we have assumed that the angular momentum distribution is cylindrically symmetric about the surface normal \hat{n} in identifying the moments appearing in Eq. (3) as the real moments of the distribution. If this assumption is incorrect or breaks down under some circumstances, other terms can contribute to Eq. (3), and the calculated $A_{0+}^{(2)}$ and $A_{0+}^{(4)}$ moments may not be the real $A_{0+}^{(2)}$ and $A_{0+}^{(4)}$ moments but could be “apparent” $A_{0+}^{(2)}$ and $A_{0+}^{(4)}$ moments.^{25,29}

In three-dimensional space, the $(JM | J_{q\pm}^{(k)} | JM)$ which are used in Eq. (1) to describe the distribution are, of course, linearly independent. However, by probing with linearly polarized light, the electric field of which is varied only within a plane, we project the $(JM | J_{q\pm}^{(k)} | JM)$ onto this plane and the resulting functions are no longer linearly independent. Thus, the terms in the sum in Eq. (3) are actually the apparent moments, which are simple sums of several real moments.^{25,29} For a fixed geometry, five apparent moments can contribute to the intensity. In addition to the three terms used in this paper, two more apparent moments of the form $A_{1+}^{(2)}$ and $A_{1+}^{(4)}$ are linearly independent and could be detected. We find that including these terms does not improve the quality of the fit to experiment. We can place upper limits of $A_{1+}^{(2)} < 0.04$ and $A_{1+}^{(4)} < 0.02$ on the value of these moments.

Unfortunately, the contribution of the other noncylindrically symmetric terms cannot be tested experimentally with linearly polarized light propagating in a fixed direction probing only one rotational branch. This needs to be emphasized. It is not simply a matter of acquiring better data and looking for a statistical breakdown in the fit [which would reveal the contribution of $A_{+1}^{(2)}$ (app) and $A_{+1}^{(4)}$ (app) terms]. Instead, one of the three constraints just stated must

TABLE II. Apparent moments as a function of the real moments for O and P branch excitation of $J = 15$ and expressions for the noncylindrically symmetric alignment moments appearing in these expansions.

O branch	
$A_{0+}^{(0)}$ (app)	$= A_{0+}^{(0)} - 0.4475A_{2+}^{(2)} + 0.0846A_{2+}^{(4)} + 0.2239A_{4+}^{(4)}$
$A_{0+}^{(2)}$ (app)	$= A_{0+}^{(2)} - 0.5744A_{2+}^{(2)} - 0.5459A_{2+}^{(4)} + 0.4127A_{4+}^{(4)}$
$A_{0+}^{(4)}$ (app)	$= A_{0+}^{(4)} - 0.8944A_{2+}^{(4)} + 0.1690A_{4+}^{(4)}$
P branch	
$A_{0+}^{(0)}$ (app)	$= A_{0+}^{(0)} + 0.1398A_{2+}^{(2)} - 0.2856A_{2+}^{(4)} - 0.7556A_{4+}^{(4)}$
$A_{0+}^{(2)}$ (app)	$= A_{0+}^{(2)} - 0.5744A_{2+}^{(2)} - 5.8975A_{2+}^{(4)} + 4.4567A_{4+}^{(4)}$
$A_{0+}^{(4)}$ (app)	$= A_{0+}^{(4)} - 0.8944A_{2+}^{(4)} + 0.1690A_{4+}^{(4)}$
$A_{2+}^{(2)}$	$= (3)^{(1/2)} \langle (J_x (J_x^2 - J_y^2) J_x) \rangle$
$A_{2+}^{(4)}$	$= [(5)^{1/2}/4] \langle (J_x (J_x^2 - J_y^2)^2 + J_y^2 + J_x - J_x) J_x \rangle$
$A_{4+}^{(4)}$	$= [(35)^{1/2}/8] \langle (J_x + J_x - J_x - J_x) J_x \rangle$

be relaxed. We must (1) vary the laser propagation direction (difficult at best for elaborate beam–surface scattering experiments), (2) analyze data from multiple rotational branches, or (3) probe the sample with circular or elliptically polarized light. The third possibility turns out to be a poor way to determine alignment because elliptically polarized light is sensitive to $A_q^{(k)}$ moments in which k is odd, i.e., orientation moments. This topic is the subject of another publication.³⁰ In what follows we detail an analysis based on the second approach and consider the effect noncylindrical symmetry could have on our results.

In Table II we present expressions for the apparent moments $A_{0+}^{(0)}$ (app), $A_{0+}^{(2)}$ (app), and $A_{0+}^{(4)}$ (app) in terms of the real moments of the distribution for $J = 15$. Also listed in Table II are expressions for the $A_{2+}^{(2)}$, $A_{2+}^{(4)}$, and $A_{4+}^{(4)}$ terms; these terms measure projections and correlations of \mathbf{J} on and in the x – y plane (where z is again along the surface normal). Based on the general perception of the Ag(111) surface as flat and on the fact that most of our experiments are done at angles of incidence relatively close to the surface normal, we would expect these terms to be small relative to terms measuring J_z .

Inspection of the terms in Table II indicates that by measuring two rotational branches we can estimate the contribution of $A_{2+}^{(4)}$ and $A_{4+}^{(4)}$ since the coefficients of these two terms are very different in the expressions for $A_{0+}^{(2)}$ (app). To pursue this, we analyze our polarization data as follows: the data from the O and P branches are fit jointly to find $A_{0+}^{(4)}$ (app) and then fit separately (with the value of $A_{0+}^{(4)}$ fixed) to obtain two estimates for $A_{0+}^{(2)}$ (app). The results are shown in Fig. 13 for the same data shown in Fig. 5. The data show a small but systematic difference, indicating a likely contribution from the $A_{2+}^{(4)}$ and $A_{4+}^{(4)}$ terms. It is not possible to find the individual values of these moments because the system is underdetermined.

However, we can estimate the magnitude of the x – y plane asymmetry that would be required. We model the distribution classically so that \mathbf{J} is constrained to be perpendicular to the surface normal and to be distributed as an ellipse in the x – y plane: $P(\varphi) = a^2 \cos^2 \varphi + b^2 \sin^2 \varphi$ where φ is the angle that \mathbf{J} makes with the x axis. We choose $a = 0.25$ and $b = 0.50$ giving a cigar-shaped distribution directed along

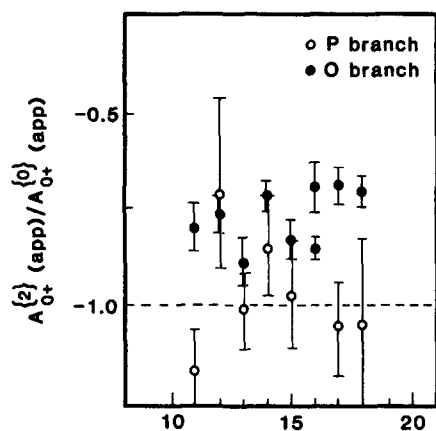


FIG. 13. Quadrupole alignment moments, $A_{0+}^{(2)}$ (app), determined separately from O and P branch excitation of the type of measurement shown in Fig. 3.

the y axis which is normalized to unity. For $J = 15$, we get for the real moments: $A_{0+}^{(0)} = 1.0$; $A_{0+}^{(2)} = -1.0$; $A_{0+}^{(4)} = 0.375$; $A_{2+}^{(2)} = -0.058$; $A_{2+}^{(4)} = +0.027$; and $A_{4+}^{(4)} = 0.0$. Then the apparent moments calculated from Table II are: $A_{0+}^{(0)}$ (app, O branch) = 1.03; $A_{0+}^{(0)}$ (app, P branch) = 0.98; $A_{0+}^{(2)}$ (app, O branch) = -0.93 (O branch); $A_{0+}^{(2)}$ (app, P branch) = -1.14 (P branch); $A_{0+}^{(4)}$ (app, O) = +0.35; and $A_{0+}^{(4)}$ (app, P) = +0.32. [Note: the apparent $A_{0+}^{(k)}$ moments are different for the O and P branches even though the equations in Table II are identical because the moments are reduced (divided) by the (apparent) value of $A_{0+}^{(0)}$.^{25,29}] From this we conclude: (1) $A_{0+}^{(0)}$ (app) is not very sensitive to noncylindrical symmetry; (2) the difference between the real $A_{0+}^{(2)}$ (app) and $A_{0+}^{(2)}$ (app, O branch) is small and is on the order of the uncertainty in our measurements; (3) $A_{0+}^{(4)}$ (app) from both branches is a good measure of $A_{0+}^{(4)}$ (real); and (4) the difference between $A_{0+}^{(2)}$ (app) for the O and P branches is a good check on the presence of noncylindrical symmetry. We also see that an anisotropy in the J distribution in the x - y plane can account for the observed discrepancy between the $A_{0+}^{(2)}$ (app) moments determined from different branches and may explain the decrease in $A_{0+}^{(2)}$ (app) at high J seen in Fig. 4.

In the joint fits presented in this paper, the $A_{0+}^{(2)}$ value tends to be largely determined by the O branch and $A_{0+}^{(4)}$ by the P branch because the associated $P_{0+}^{(k)}$ lines strengths are 2-3 times larger.^{25,29} Therefore, we conclude that the moments presented in Figs. 5 and 6 are good estimates of the real $A_{0+}^{(2)}$ and $A_{0+}^{(4)}$ moments.

¹C. W. Muhlhhausen, L. R. Williams, and J. C. Tully, *J. Chem. Phys.* **83**, 2594 (1985).

²T. R. Proctor, D. J. Kouri, and R. B. Gerber, *J. Chem. Phys.* **80**, 3845 (1984); H. R. Mayne, C.-Y. Kuan, and R. J. Wolf, *Chem. Phys. Lett.* **140**, 520 (1987); H. R. Mayne, *J. Chem. Phys.* **88**, 7424 (1988).

³J. A. Barker and D. J. Auerbach, *Surf. Sci. Rep.* **4**, 1 (1984).

⁴D. S. King and R. R. Cavanagh, in *Chemistry and Structure of Interfaces*, edited by R. B. Hall and A. B. Ellis (VCH, Deerfield Beach, FL, 1986).

⁵M. C. Lin and G. Ertl, *Annu. Rev. Phys. Chem.* **37**, 587 (1986).

⁶G. M. McClelland, G. D. Kubiak, H. G. Rennagel, and R. N. Zare, *Phys. Rev. Lett.* **46**, 831 (1981).

⁷A. W. Kleyn, A. C. Luntz, and D. J. Auerbach, *Phys. Rev. Lett.* **47**, 1169 (1981).

⁸A. W. Kleyn, A. C. Luntz, and D. J. Auerbach, *Surf. Sci.* **117**, 33 (1982).

⁹A. C. Luntz, A. W. Kleyn, and D. J. Auerbach, *Phys. Rev. B* **25**, 4273 (1982).

¹⁰A. W. Kleyn, A. C. Luntz, and D. J. Auerbach, *Surf. Sci.* **152/153**, 99 (1985).

¹¹G. D. Kubiak, J. E. Hurst, H. G. Rennagel, G. M. McClelland, and R. N. Zare, *J. Chem. Phys.* **79**, 5163 (1983).

¹²A. C. Luntz, A. W. Kleyn, and D. J. Auerbach, *J. Chem. Phys.* **76**, 737 (1982).

¹³D. C. Jacobs, K. W. Kolasinski, R. J. Madix, and R. N. Zare, *J. Chem. Phys.* **87**, 5038 (1987).

¹⁴L. J. F. Hermans, J. J. G. M van der Tol, and J. J. M. Beenakker, *J. Chem. Phys.* **84**, 1029 (1986).

¹⁵C. W. Muhlhhausen, J. A. Serri, J. C. Tully, G. E. Becker, and M. J. Cardillo, *Isr. J. Chem.* **22**, 315 (1982).

¹⁶H. Asada, *Jpn. J. Appl. Phys.* **20**, 527 (1981).

¹⁷H. Asada and T. Matsui, *Jpn. J. Appl. Phys.* **21**, 259 (1982).

¹⁸J. C. Tully, C. W. Muhlhhausen, and L. R. Ruby, *Ber. Bunsenges. Phys. Chem.* **86**, 433 (1982).

¹⁹G. O. Sitz, A. C. Kummel, and R. N. Zare, *J. Chem. Phys.* **87**, 3247 (1987).

²⁰G. O. Sitz, A. C. Kummel, and R. N. Zare, *J. Vac. Sci. Technol. A* **5**, 513 (1987).

²¹G. D. Kubiak, G. O. Sitz, and R. N. Zare, *J. Chem. Phys.* **83**, 2538 (1985).

²²B. D. Kay, T. D. Raymond, and J. K. F. Rice, *Rev. Sci. Instrum.* **57**, 2266 (1986).

²³K. L. Carleton, S. R. Leone, and K. H. Welge, *Chem. Phys. Lett.* **115**, 492 (1985).

²⁴J. T. Vanderslice, S. G. Tilford, and P. G. Wilkerson, *Astrophys. J.* **141**, 395 (1965).

²⁵A. C. Kummel, G. O. Sitz, and R. N. Zare, *J. Chem. Phys.* **85**, 6874 (1986). Equations (2) and (3) are valid only for linearly polarized light traveling along the $-y$ axis.

²⁶K. Blum, *Density Matrix Theory and Applications* (Plenum, New York, 1981).

²⁷In the symbols $Y_{q\pm}^{(k)}$ and $A_{q\pm}^{(k)}$ the brackets around k and the $+$ or $-$ symbol after the q indicates that we are employing the Hertel-Stoll²⁸ notation for the spherical tensors. In this normalization all the spherical tensors are real.

²⁸I. V. Hertel and W. Stoll, *Adv. At. Mol. Phys.* **13**, 113 (1978).

²⁹A. C. Kummel, G. O. Sitz, and R. N. Zare, *J. Chem. Phys.* **88**, 6707 (1988).

³⁰G. O. Sitz, A. C. Kummel, R. N. Zare, and J. C. Tully, *J. Chem. Phys.* **89**, 2572 (1988).

³¹C.-Y. Kuan, H. R. Mayne, and R. J. Wolf, *Chem. Phys. Lett.* **133**, 415 (1987).

³²J. G. Lauderdale, J. F. McNutt, and C. W. McCurdy, *Chem. Phys. Lett.* **107**, 43 (1984).

³³G. C. Corey and M. H. Alexander, *J. Chem. Phys.* **87**, 4937 (1987).

³⁴J. E. Smedley, G. C. Corey, and M. H. Alexander, *J. Chem. Phys.* **87**, 3218 (1987).

³⁵R. J. Wolf, D. C. Collins, Jr., and H. R. Mayne, *Chem. Phys. Lett.* **119**, 533 (1985).

³⁶C. H. Greene and R. N. Zare, *J. Chem. Phys.* **78**, 6741 (1983).

³⁷C. T. Rettner, J. Kimman, F. Fabre, D. J. Auerbach, J. A. Barker, and J. C. Tully, *J. Vac. Sci. Technol. A* **5**, 508 (1987).

³⁸F. Budde, A. Mödl, A. V. Hamza, P. M. Ferm, and G. Ertl, *Surf. Sci.* **192**, 507 (1987).

³⁹K. C. Janda, J. E. Hurst, J. P. Cowin, L. Wharton, and D. J. Auerbach, *Surf. Sci.* **130**, 395 (1983).

⁴⁰J. E. Hurst, L. Wharton, K. C. Janda, and D. J. Auerbach, *J. Chem. Phys.* **78**, 1559 (1983).

⁴¹J. P. Cowin, C. F. Yu, S. J. Sibener, and L. Wharton, *J. Chem. Phys.* **79**, 3537 (1983).

⁴²R. J. Hamers, P. L. Houston, and R. P. Merrill, *J. Chem. Phys.* **83**, 6045 (1985).